Earth and Planetary Science Letters 487 (2018) 165–178

Contents lists available at ScienceDirect

Earth and Planetary Science Letters

www.elsevier.com/locate/epsl

Formation of fast-spreading lower oceanic crust as revealed by a new Mg–REE coupled geospeedometer

Chenguang Sun [a,b,*], C. Johan Lissenberg [c]

[a] Department of Earth, Environmental and Planetary Sciences, Rice University, USA
[b] Department of Geology and Geophysics, Woods Hole Oceanographic Institution, USA
[c] School of Earth and Ocean Sciences, Cardiff University, UK

ARTICLE INFO

Article history:
Received 7 October 2017
Received in revised form 26 January 2018
Accepted 29 January 2018
Available online 12 February 2018
Editor: M. Bickle

Keywords:
oceanic crust
cooling rate
crystallization temperature
plagioclase
clinopyroxene
Hess Deep

ABSTRACT

A new geospeedometer is developed based on the differential closures of Mg and rare earth element (REE) bulk-diffusion between coexisting plagioclase and clinopyroxene. By coupling the two elements with distinct bulk closure temperatures, this speedometer can numerically solve the initial temperatures and cooling rates for individual rock samples. As the existing Mg-exchange thermometer was calibrated for a narrow temperature range and strongly relies on model-dependent silica activities, a new thermometer is developed using literature experimental data. When the bulk closure temperatures of Mg and REE are determined, respectively, using this new Mg-exchange thermometer and the existing REE-exchange thermometer, this speedometer can be implemented for a wide range of compositions, mineral modes, and grain sizes.

Applications of this new geospeedometer to oceanic gabbros from the fast-spreading East Pacific Rise at Hess Deep reveal that the lower oceanic crust crystallized at temperatures of 998–1353 °C with cooling rates of 0.003–10.2 °C/yr. Stratigraphic variations of the cooling rates and crystallization temperatures support deep hydrothermal circulations and in situ solidification of various replenished magma bodies. Together with existing petrological, geochemical and geophysical evidence, results from this new speedometry suggest that the lower crust formation at fast-spreading mid-ocean ridges involves emplacement of primary mantle melts in the deep section of the crystal mush zone coupled with efficient heat removal by crustal-scale hydrothermal circulations. The replenished melts become chemically and thermally evolved, accumulate as small magma bodies at various depths, feed the shallow axial magma chamber, and may also escape from the mush zone to generate off-axial magma lenses.

1. Introduction

Earth's lower oceanic crust is mainly composed of mafic cumulate rocks (e.g., gabbros and gabbronorites), solidifying from mantle-derived melts beneath the spreading mid-ocean ridges. This cumulate section thus records styles of igneous accretion and crustal cooling. Many crustal formation models have been proposed based on petrological observations, deformation structures, and geodynamic simulations at various ocean ridge settings and ophiolites (e.g., Nicolas et al., 1988; Phipps Morgan and Chen, 1993; Quick and Denlinger, 1993; Kelemen et al., 1997; Dick et al., 2008). Among these, two end-member models for fast spreading mid-ocean ridges are actively debating whether cumulates of the lower oceanic crust crystalize mainly in a shallow melt lens (e.g., Phipps Morgan and Chen, 1993; Quick and Denlinger, 1993; Coogan et al., 2007; Faak et al., 2015) or *in situ* solidify largely from magma sills at various depths (e.g., Nicolas et al., 1988; Kelemen et al., 1997; Lissenberg et al., 2004; Maclennan et al., 2005; VanTongeren et al., 2008, 2015; Natland and Dick, 2009). The former postulates much slower cooling in the deeper crust (i.e., near-conductive cooling), whereas the latter necessitates efficient heat removal by hydrothermal circulations throughout the entire crust. Thus, a key to distinguishing these two models is the cooling history of the lower crust at fast-spreading mid-ocean ridges.

Geospeedometers have the ability to extract cooling information of natural rocks from mineral compositions using analytical or numerical models (e.g., Dodson, 1973; Eiler et al., 1992; Ganguly and Tirone, 1999; Costa et al., 2003; Müller et al., 2013; Watson and Cherniak, 2015; Liang, 2017). Applying the closure temperature equation of Dodson (1973) to Ca in olivine, two research groups estimated cooling rates of oceanic gabbros from the

* Corresponding author at: Department of Earth, Environmental and Planetary Sciences, Rice University, USA.
E-mail address: csun@rice.edu (C. Sun).

https://doi.org/10.1016/j.epsl.2018.01.032

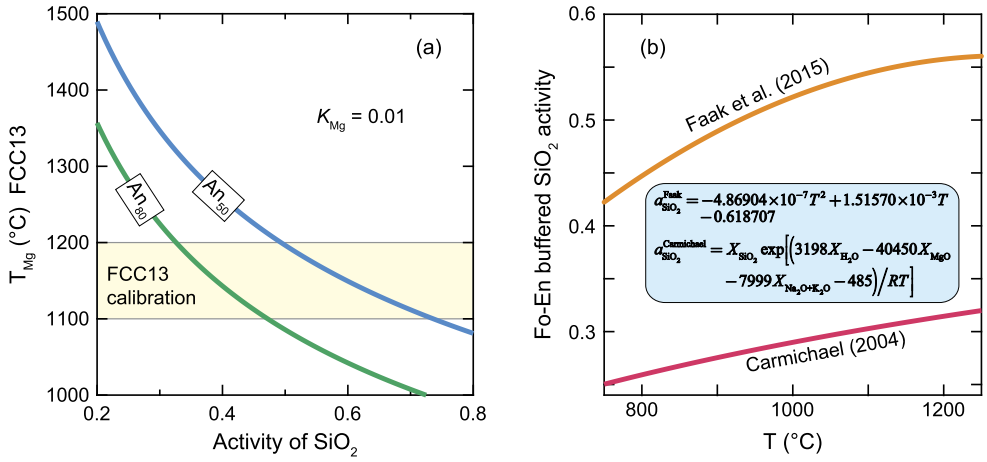

Fig. 1. Plots showing (a) the variations of temperatures (T_{Mg}) calculated using the plagioclase–clinopyroxene Mg-exchange thermometer of Faak et al. (2013) as a function of silica activity and (b) the differences of two existing silica activity models for a basaltic system. Light yellow region in (a) indicates the temperature calibration range for the thermometer of Faak et al. (2013). A fixed Mg partition coefficient (K_{Mg} = 0.01) and two plagioclase compositions (An_{50} and An_{80}; An_{50} denotes 50 mol% anorthite in plagioclase) were used in (a). Inset in (b) shows the silica activity model expressions of Faak et al. (2015) and Carmichael (2004), in which T is temperature in K, R is the gas constant, and X denotes the oxide molar fraction. The melt in (b) used for Carmichael's model has a typical basaltic composition (i.e., 022005-1522 used in Faak et al., 2013). (For interpretation of the references to color in this figure legend, the reader is referred to the web version of this article.)

Oman ophiolite, an analogue of fast-spreading mid-ocean ridges, but obtained highly controversial results: one showed slower cooling rates consistent with near-conductive cooling (e.g., Coogan et al., 2007), whereas the other found higher cooling rates supporting deep hydrothermal cooling (VanTongeren et al., 2008). The reasons for their discrepancies remain unclear, but their approaches may involve uncertainties arising from the Dodson-type assumptions: (1) negligible influences of initial temperatures and (2) surrounding clinopyroxene acting as an infinite reservoir.

Using their newly developed Mg-in-plagioclase geospeedometer, Faak et al. (2015) argued that cooling rates derived from their 1-D grain-scale diffusion modeling support near-conductive cooling of the lower crust at the East Pacific Rise (EPR). However, in addition to the Dodson-type assumptions, results of Faak et al. (2015) are also likely subject to uncertainties from their Mg-exchange thermometer (Faak et al., 2013) and 1-D plane sheet approximation. Particularly, Faak et al.'s thermometer has a strong dependence upon silica activities that can only be calculated using existing activity models (Fig. 1a–b). Silica activities in a typical basaltic system buffered by olivine and orthopyroxene appear to differ by a factor of two between the models of Faak et al. (2015) and Carmichael (2004) (Fig. 1b), corresponding to 100–200 °C differences in Faak et al.'s thermometer (cf. Fig. 1a). Because Faak et al.'s thermometer was calibrated only at 1100–1200 °C for plagioclase with 50–80 mol% anorthite, it is unclear how accurately their thermometer can be extrapolated to lower temperatures (e.g., 700–900 °C; Faak et al., 2015), at which Mg in gabbros has been extensively reset by diffusion. Although the 1-D plane sheet diffusion model is easy to implement, it is likely inadequate for 3-D shaped crystals with substantial diffusive resetting (e.g., Ganguly and Tirone, 1999; Costa et al., 2003).

In this study, we present a new Mg–REE coupled speedometer for plagioclase- and clinopyroxene-bearing rocks that could overcome the aforementioned limitations regarding the Dodson-type assumptions, silica activities, applicable temperatures and 1-D geometry. Using the bulk closure temperatures of REE and Mg, this speedometer can simultaneously determine the initial temperatures and cooling rates of individual samples. The bulk closure temperatures of REE can be calculated using the REE-exchange thermometer of Sun and Liang (2017), while those of Mg can be determined using a new Mg-exchange thermometer calibrated at 800–1430 °C. Applying this speedometer to oceanic gabbros from the Hess Deep rift valley (Lissenberg et al., 2013), we show that the lower crust of EPR at Hess Deep formed by *in situ* solidification of axial and off-axial magma intrusions at various depths with efficient heat removal through crustal-scale hydrothermal circulations.

2. Developing a Mg–REE coupled speedometer

2.1. Basic concept

The basis of geospeedometry using bulk closure temperatures was initially defined by Dodson (1973) for diffusion in a single crystal and has recently been extended to polycrystalline petrological systems (e.g., Eiler et al., 1992; Ehlers and Powell, 1994; Yao and Liang, 2015; Liang, 2017). In general, the bulk closure temperature (T_c) of an element of interest (j) in two coexisting minerals (α and β) can be described as,

$$T_c^j = f\left(T_0, dT/dt, G_{\alpha/\beta}^j\right), \tag{1a}$$

$$G_{\alpha/\beta}^j = \left\{D_\alpha^j, D_\beta^j, K_{\alpha/\beta}^j, \phi_\alpha, \phi_\beta, L_\alpha, L_\beta\right\}, \tag{1b}$$

where f denotes an unspecified expression; T_0 and dT/dt are the initial temperature and cooling rate, respectively; and G is a set of variables, including diffusion coefficients (D), partitioning coefficients (K), mineral proportions (ϕ), and grain radii (L) of the two minerals. Notably, initial temperatures of cumulate rocks can be regarded as the mean temperatures of cumulus crystallization because of their simple monotonic cooling histories subsequent to crystallization. As two elements with different diffusivities have distinct closure temperatures, when considered together the two elements could uniquely constrain both the cooling rate and initial temperature. The initial concept was briefly discussed in Sun and Liang (2017) for understanding the different temperatures derived from their REE-exchange thermometer and the Mg-exchange thermometer of Faak et al. (2013). A similar concept has also been used in Watson and Cherniak (2015) with a focus on diffusive relaxation of stepwise concentration profiles in single crystals. Here we further pursue this idea to develop a new speedometer by coupling the bulk closure temperatures of slowly diffusing REE and fast diffusing Mg in coexisting plagioclase and clinopyroxene.

In oceanic gabbros, plagioclase and clinopyroxene are the two main rock-forming minerals, co-crystallizing from the relatively dry basaltic magmas that characterize mid-ocean ridges over an extended temperature interval (e.g., Grove et al., 1992). According to

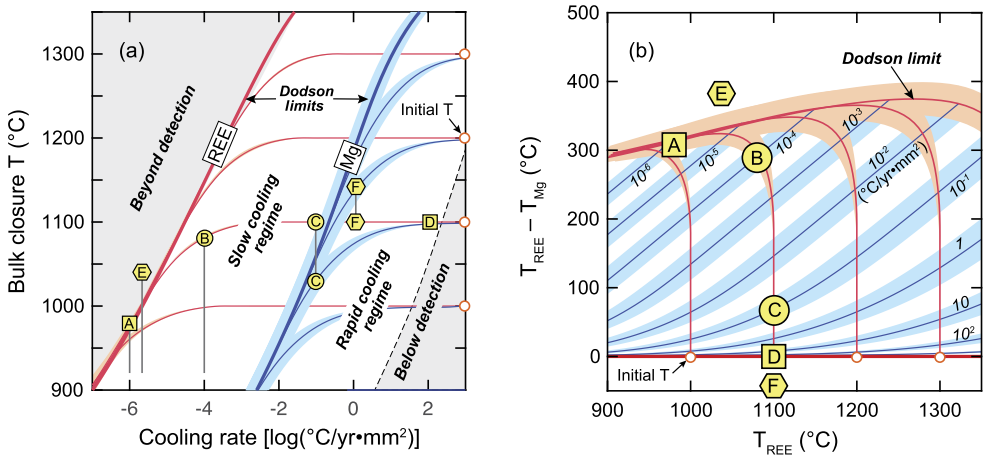

Fig. 2. Plots showing (a) bulk closure temperatures of REE (red curves) and Mg (blue curves) in a plagioclase–clinopyroxene assemblage ($\phi_{plg} = \phi_{cpx}$; $L_{plg} = L_{cpx}$) as a function of effective cooling rate (see definition in Appendix A.2) and initial temperature and (b) the differences in bulk closure temperatures between REE and Mg against REE bulk closure temperatures for four initial temperatures (thick red curves) and a range of cooling rates (thin blue curves). Error envelopes mark the uncertainties due to a factor of two variations in Mg and REE diffusivities in plagioclase (cf. Fig. A.1). Yellow markers denote six representative samples. Among them, *A*, *B*, *C*, and *D* have the same initial temperature but different cooling rates, whereas *E* and *F* indicate anomalous examples possibly due to uncertainties of the bulk closure temperatures and/or complex cooling histories. Vertical grey lines in (a) link the bulk closure temperatures of REE and Mg for the same cooling rates. The Mg bulk closure temperatures of points *A*, *B* and *E* in (a) are below the plotted temperature interval (900–1350 °C). The REE bulk closure temperature of point *D* in (a) overlaps with its Mg bulk closure temperature. (For interpretation of the references to color in this figure legend, the reader is referred to the web version of this article.)

the aforementioned concept, the bulk closure temperatures of Mg and REE in coexisting plagioclase and clinopyroxene from the same gabbro sample should follow two different equations,

$$T_c^{Mg} = f\left(T_0, dT/dt, G^{Mg}_{plg/cpx}\right), \tag{2a}$$

$$T_c^{REE} = f\left(T_0, dT/dt, G^{REE}_{plg/cpx}\right). \tag{2b}$$

Thus, the two unknowns, T_0 and dT/dt, can be solved simultaneously for individual samples through a root-finding algorithm when two conditions are met: (1) bulk closure temperatures of REE and Mg are determined accurately and (2) expressions of Eq. (2a)–(2b) are established explicitly. The REE-exchange thermometer of Sun and Liang (2017) was calibrated against experimentally determined REE partitioning data for plagioclase-melt (Sun et al., 2017) and clinopyroxene-melt systems (Sun and Liang, 2012), respectively. As demonstrated by Sun and Liang (2017), their thermometer is independently testable by volcanic samples from the literature and thus can determine REE bulk closure temperatures with confidence. A new Mg-exchange thermometer is presented in Section 2.2 for accurate constraints on Mg bulk closure temperatures. Expressions of Eq. (2a)–(2b) can then be obtained explicitly using the numerical methods in Appendix A.

To illustrate the concept and limitations of this speedometry, we performed numerical simulations for bulk diffusion in a cooling plagioclase–clinopyroxene aggregate with equal mineral modes ($\phi_{plg} = \phi_{cpx}$), uniform grain radii ($L_{plg} = L_{cpx}$). Plagioclase was assumed with 65 mol% anorthite. The imposed cooling profiles cover equilibrium initial temperatures from 1000 to 1400 °C and effective cooling rates from 10^{-7} to 10^{3} °C/yr·mm^2 (see definition in Appendix A.2). Potential errors due to diffusivities were examined by assigning a factor of two uncertainties to REE and Mg diffusion coefficients in plagioclase (cf. Fig. A.1). The diffusivity uncertainties do not result in obvious variations in the bulk closure temperatures of slowly-diffusing REE (orange envelopes in Fig. 2a), but give rise to ~0–20 °C variations in the bulk closure temperatures of fast-diffusing Mg (blue envelopes in Fig. 2a). The small variations of Mg closure temperatures correspond to about a factor of two errors in cooling rates (blue envelopes in Fig. 2b). In Fig. 2a, bulk closure temperatures of REE (red curves) and Mg (blue curves) can be divided into two characteristic regimes (slow- and fast-cooling regimes, respectively) according to their responses to cooling rates (Fig. 2a). Boundaries of these two regimes correspond to the bulk closure temperatures for a "sufficiently high initial temperature". This initial condition was first used in Dodson (1973) to formulate closure temperatures in single crystals. For this historical reason, here we defined the two boundaries as the *Dodson limits*. Note that the Dodson limit for an element of interest should also varies with dT/dt and G (Eq. (2a)–(2b)).

The upper boundary in Fig. 2b shows maximum differences in the bulk closure temperatures between REE and Mg and effectively represents the Dodson limit of REE. Along the Dodson limit of REE (e.g., point *A* in Fig. 2b), both Mg and REE bulk closure temperatures lose the memory of initial conditions (red curves in Fig. 2b), so they could only constrain accurate cooling rates (blue curves in Fig. 2b) and lower limits of initial temperatures. Below the Dodson limit of REE (e.g., points *B* and *C* in Fig. 2b), the bulk closure temperatures of Mg and REE can partially retain memories of initial conditions and cooling rates, and therefore coupling the two could uniquely solve the cooling path. For very rapid cooling (e.g., point *D* in Fig. 2b), bulk closure temperatures of Mg and REE may only record initial conditions with lower limits of cooling rates. When the bulk closure temperatures of Mg and REE in a polycrystalline sample can be accurately constrained using exchange thermometers, one could use Fig. 2b to determine the initial temperature and cooling rate together. However, this new speedometer is unsuitable for samples beyond the Dodson limit of REE (e.g., point *E* in Fig. 2b) or below the initial temperature (e.g., point *F* in Fig. 2b), which possibly have inaccurate estimations of bulk closure temperatures and/or more complex thermal histories. Through Monte Carlo simulations (Fig. S1), we found that uncertainties of the initial temperatures are mainly from REE bulk closure temperatures while those of the cooling rates are mostly from Mg bulk closure temperatures. When the closure temperatures approach the Dodson limit in Fig. 2b, uncertainties of the initial temperatures become significantly greater due to errors in Mg bulk closure temperatures (cf. Fig. S1b).

Because the mineral mode, grain size, and composition-dependent diffusion and partition coefficients all together determine the diffusive exchange between plagioclase and clinopyroxene (Appendix A), applications of this Mg–REE coupled speedometry require a substantial amount of numerical simulations to constrain the exact relations between bulk closure temperatures

and cooling rates for individual samples as shown in Fig. 2. To reduce the numerical calculations for individual cases, we ran 1.575×10^5 diffusion simulations and calculated the bulk closure temperatures of Mg and REE for a wide range of initial temperatures (700–1400 °C), cooling rates (10^{-7}–10^6 °C/yr·mm^2), plagioclase compositions (An_{29-87}), mineral proportions ($\phi_{plg}/\phi_{cpx} = 0.01-100$), and grain radii ($L_{plg}/L_{cpx} = 0.1-10$). The numerical solutions were collected in a multi-dimensional grid that can be used to interpolate the expressions of Eq. (2a)–(2b) for inverse calculations of initial temperatures and cooling rates. A simple Matlab® script is provided in the Supplementary Materials for interested users to automate these inverse calculations using our numerical solutions. In the following sub-sections, we first calibrate a new Mg-exchange thermometer and then show the effects of plagioclase composition, mineral proportion, and grain radius on the bulk closure temperatures of Mg and REE.

2.2. Calibration of a new Mg-exchange thermometer

2.2.1. Calibration strategy

The basis of an exchange thermometer is the temperature-sensitive exchange reaction for an element of interest between coexisting minerals. Here we suggest that Mg exchange between plagioclase (plg) and clinopyroxene (cpx) is coupled with Ca through the following reaction,

$$\left[Mg^*\right]_{cpx} + [CaAl_2Si_2O_8]_{plg} = \left[Ca^*\right]_{cpx} + [MgAl_2Si_2O_8]_{plg}, \quad (3a)$$

where $[Mg^*]_{cpx}$ and $[Ca^*]_{cpx}$ indicate Mg- and Ca-bearing end-member components in clinopyroxene (e.g., $-Al_2SiO_6$, $-MgSi_2O_6$, or $-CaSi_2O_6$). This reaction does not imply a negligible effect of silica activities on Mg partitioning. Although not directly measurable in natural petrological systems, silica activities may influence the mineral major compositions as well as the equilibrium phase relations, for instance, through

$$[CaAl_2Si_2O_8]_{plg} = [SiO_2] + [CaAl_2SiO_6]_{cpx}. \quad (3b)$$

An obvious advantage of Eq. (3a) is that it can simply describe Mg exchange without involving activity terms or additional phases, which allows the development of a new Mg-exchange thermometer independent of silica activities.

According to Eq. (3a), the Mg partition coefficient (K_{Mg}) can be described as

$$\ln K_{Mg} = \ln\left(\frac{C^{plg}_{Mg^*}}{C^{cpx}_{Mg^*}}\right) = -\frac{\Delta H + P\Delta V}{RT} + \frac{\Delta S}{R} - \ln\left(\frac{a^{cpx}_{Ca^*}}{a^{plg}_{Ca^*}}\frac{\gamma^{plg}_{Mg^*}}{\gamma^{cpx}_{Mg^*}}\right), \quad (4a)$$

where ΔH, ΔV, and ΔS, are changes of enthalpy, volume, and entropy, respectively, for the exchange reaction; a_{Ca^*} is the activity of a Ca-bearing component; γ_{Mg^*} is the activity coefficient of a Mg-bearing component; C_{Mg^*} is the concentration of a Mg-bearing component; and P is pressure. The activity of Ca-component in plagioclase (i.e., anorthite) is a function of temperature and anorthite content in plagioclase (e.g., Holland and Powell, 1992). A similar function may also be applicable for the activity coefficient of Mg-component in plagioclase. If a_{Ca^*} and γ_{Mg^*} in clinopyroxene are less important, Eq. (4a) can be simplified as

$$\ln K_{Mg} = b_0 + \frac{b_1 + b_2 \times P}{T} + f(X_{An}), \quad (4b)$$

where b_0, b_1, and b_2 are coefficients corresponding to $\Delta S/R$, $-\Delta H/R$, and $-\Delta V/R$, respectively; X_{An} is the anorthite content in plagioclase [$X_{An} = Ca/(Ca + Na + K)$, in molar unit]; and $f(X_{An})$ is a composition correction term for a_{Ca^*} and γ_{Mg^*} in plagioclase and likely follows a quadratic expression (e.g., Holland and Powell, 1992; Sun et al., 2017).

Many phase equilibria studies experimentally produced plagioclase and clinopyroxene coexisting with silicate melts and other minerals (see Table S1). Through a routine procedure of electron microprobe analyses, Mg could be accurately determined in silicate melts and clinopyroxene but is relatively more difficult to measure in plagioclase, because Mg is highly incompatible in plagioclase. Thus, the data qualities of Mg in plagioclase are not uniform among existing phase equilibria studies. This issue, however, can be eliminated if reliable plagioclase-melt Mg partition coefficients are available for individual experiments. Recently, Sun et al. (2017) developed a new set of parameterized lattice strain models for trace element partitioning between plagioclase and silicate melt. They showed that their models not only reproduce experimental partitioning data (1127–1410 °C; $X_{An} = 0.41-0.98$) better than previous models but are also testable by phenocryst-melt partitioning data (1000–1216 °C; $X_{An} = 0.29-0.82$). With the partitioning model of Sun et al. (2017), we can then use existing phase equilibria data to calibrate the plagioclase–clinopyroxene Mg partitioning model (Eq. (4b)).

2.2.2. Calibration results and model tests

We used the LEPR database of experimental studies (http://lepr.ofm-research.org) as guidance and selected 43 phase equilibria studies that reported coexisting plagioclase, clinopyroxene, and silicate melt. To minimize kinetic effects on major elements (e.g., Al and Si) in plagioclase and clinopyroxene, we excluded experiments that were conducted at low temperatures for short durations (i.e., <24 h at ≤1100 °C, and <12 h at ≤1250 °C). Experiments with less than 0.5 wt% MgO in silicate melts were also excluded to avoid possibly large analytical errors. After filtering, we obtained 304 experiments that cover a broad range of temperatures (800–1430 °C), pressures (1 atm–2.7 GPa), and compositions (melt SiO_2 = 40–74 wt%; plagioclase An = 28–100; clinopyroxene Mg# = 26–100, where An = 100 × X_{An} and Mg# = 100 × Mg/(Mg + Fe), in molar unit; see details in Table S1). Using the partitioning model of Sun et al. (2017), we calculated plagioclase-melt Mg partition coefficients (0.009–0.047) for individual experiments and then obtained MgO contents in plagioclase from the reported MgO abundances in silicate melts. The melt-derived MgO concentrations in plagioclase (0.007–0.550) are generally smaller than the reported MgO data of plagioclase by about a factor of 1.5 (see Table S1).

Through multiple linear regression analyses of the plagioclase–clinopyroxene Mg partition coefficients, we determined the explicit expression of Eq. (4b) through two steps. First, we excluded the 8 silica-saturated experiments in our initial calibration but found that this initial model can well reproduce the silica-saturated Mg partitioning data. Thus, including these silica-saturated experiments in our final calibration, we obtained the following expression to describe Mg partitioning between plagioclase and clinopyroxene,

$$\ln K_{Mg} = 5.15(\pm 0.27) - \frac{14265(\pm 369) + 487(\pm 38)P^2}{T} + 0.75(\pm 0.10)X^2_{An}, \quad (5)$$

where T is temperature in K; P is pressure in GPa; and uncertainties in parentheses are 1σ directly obtained from the regression. A second order pressure term appears to be necessary to better fit the Mg partitioning data, but pressure is insignificant under oceanic crustal conditions (≤2 kbar). Re-arranging Eq. (5) gives the following expression for a new thermometer based on Mg exchange between plagioclase and clinopyroxene,

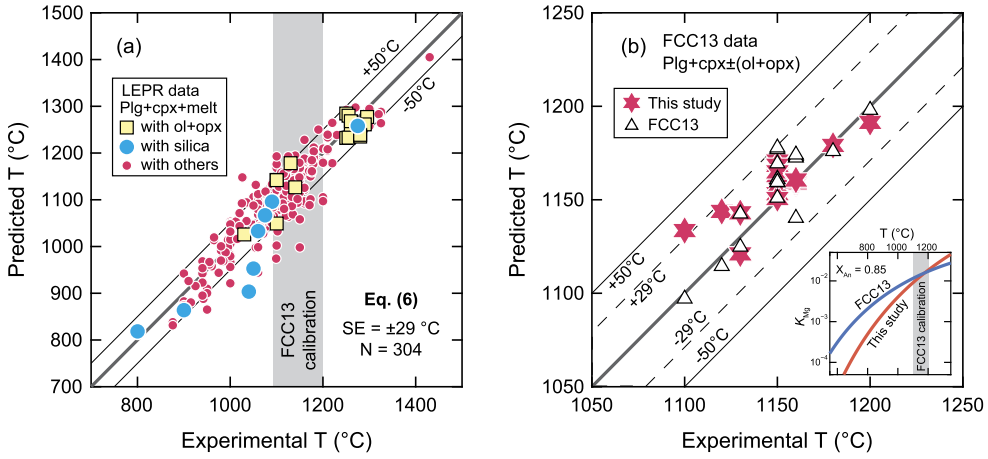

Fig. 3. Comparisons between experimental temperatures and thermometer-predicted values for 304 phase equilibria experiments from 43 studies in the literature (a) and for 18 diffusion experiments from Faak et al. (2013) (b). Grey regions in (a) and (b) indicate the temperature calibration range of the thermometer of Faak et al. (2013). Predicted temperatures in (a) were calculated using the thermometer of this study (Eq. (6)), while those in (b) were calculated using two different thermometers (this study vs. Faak et al., 2013). Inset in (b) displays the distinct temperature dependences between the two thermometers for a given plagioclase ($X_{An} = 0.85$). Note that the gabbro-relevant partitioning data of Faak et al. (2013) were used as independent tests of our new thermometer. SE in (a) denotes the standard error of our new thermometer (Eq. (6)). See Table S1 for details of the phase equilibria experiments used for our thermometer calibration. (For interpretation of the references to color in this figure legend, the reader is referred to the web version of this article.)

$$T(K) = \frac{14265(\pm 369) + 487(\pm 38)P^2}{-\ln K_{Mg} + 5.15(\pm 0.27) + 0.75(\pm 0.10)X_{An}^2}. \quad (6)$$

Fig. 3a shows that Eq. (6) reproduces the wide range of temperatures (800–1430 °C) for all 304 experiments to within ±50 °C regardless of the mineral assemblages (olivine, orthopyroxene, quartz, and others including amphibole, garnet, mica, ilmenite, rutile, and spinel) coexisting with plagioclase, clinopyroxene and melt. The absolute differences between the experimental temperatures and the thermometer-derived values average 29 °C, indicating the standard error of this new thermometer.

Given the diverse compositions and phase assemblages of the 304 experiments, it is difficult to estimate the silica activities of all experiments and to make a fair comparison between this thermometer and the silica activity-dependent thermometer of Faak et al. (2013). To further test this new thermometer for *gabbroic systems*, we applied it to the silica-free partitioning data of Faak et al. (2013), which were determined from 18 diffusion experiments with plagioclase crystals surrounded by clinopyroxene or gabbro powders. Importantly, for the 18 diffusion experiments, temperatures calculated using Eq. (6) agree well with the run temperatures (red hexagrams in Fig. 3b). The relative differences between these two are within the standard error of our new thermometer and are also comparable to the calibration uncertainties of the thermometer of Faak et al. (2013 white triangles in Fig. 3b). This establishes an independent validation of this new thermometer particularly for applications to ocean gabbros. Although consistent with our new thermometer at 1100–1200 °C, Faak et al.'s thermometer generates systematically lower temperatures at <1100 °C due to excessive extrapolations (see inset in Fig. 3b).

2.3. Effects of mineral composition, size, and volume on bulk closure temperatures

Following the numerical methods described in Appendix A, we simulated the bulk closure temperatures of Mg and REE in cooling plagioclase–clinopyroxene aggregates for variable plagioclase compositions, mineral modes and grain sizes. For the purpose of demonstration, we used five choices of effective cooling rates (10^{-3}, $10^{-2.5}$, 10^{-2}, $10^{-1.5}$, and 10^{-1} °C/yr·mm^2; see definition in Appendix A.2) at an initial temperature of 1150 °C. The compositional effect was manifested through simulations for plagioclase with 25–90 mol% anorthite, uniform crystal sizes and equal modal proportions of plagioclase and clinopyroxene. As the effective cooling rate incorporates the variation of uniform grain size, the effect of grain sizes was analyzed numerically using simulations for differentiated crystal radii between plagioclase and clinopyroxene ($L_{plg}/L_{cpx} = 0.1$–10). The effect of mineral modes was singled out in simulations with various ratios of mineral proportions ($\phi_{plg}/\phi_{cpx} = 0.1$–100), uniform crystal sizes and plagioclase with 65 mol% anorthite. The simulation results are shown in Fig. 4.

The bulk closure temperatures of REE vary within a narrow range (< ~20 °C) near the initial cooling temperature, whereas those of Mg cover a wide range and deviate significantly from the initial temperatures (Fig. 4). In a given plagioclase–clinopyroxene aggregate, the bulk closure temperatures of Mg decrease by ~150 °C as the effective cooling rate decreases from 10^{-3} to 10^{-1} °C/yr·mm^2, indicating the sensitivity of Mg bulk closure temperatures to cooling rates. However, the bulk closure temperatures of Mg also show considerable variations with plagioclase compositions, grain radii, and mineral modes. Due to the strong dependence of Mg diffusivities on anorthite in plagioclase, Mg bulk closure temperatures increase by ~150 °C with the increase of anorthite in plagioclase from 25 to 90 mol% (Fig. 4a). When the differential grain size (L_{plg}/L_{cpx}) increases from 0.1 to 10, Mg bulk closure temperature increases by ~300 °C (Fig. 4b). Because we took clinopyroxene grain size as the reference, an increase of differential grain size simply indicates a relative increase of plagioclase grain radii and hence induces a higher Mg bulk closure temperature. As the effective cooling rate was defined as the product of actual cooling rate and the square of clinopyroxene grain radius, a larger clinopyroxene size induces a greater effective cooling rate and hence also increases the Mg bulk closure temperature. Notably, this indicates that the role of clinopyroxene size cannot be omitted for modeling Mg diffusion between plagioclase and clinopyroxene.

An increase of ~100 °C in Mg bulk closure temperatures appears when the relative mineral mode (ϕ_{plg}/ϕ_{cpx}) increases from 0.1 (clinopyroxene-rich) to 100 (plagioclase-rich) (Fig. 4c). In the two end-member cases, Mg bulk closure temperatures are mainly controlled by diffusion in the minor phases while the major ones serve as "infinite" reservoirs (e.g., Liang, 2014). Specifically, Mg bulk closure temperatures are governed by its diffusion in plagioclase for the clinopyroxene-rich end-member but by its diffu-

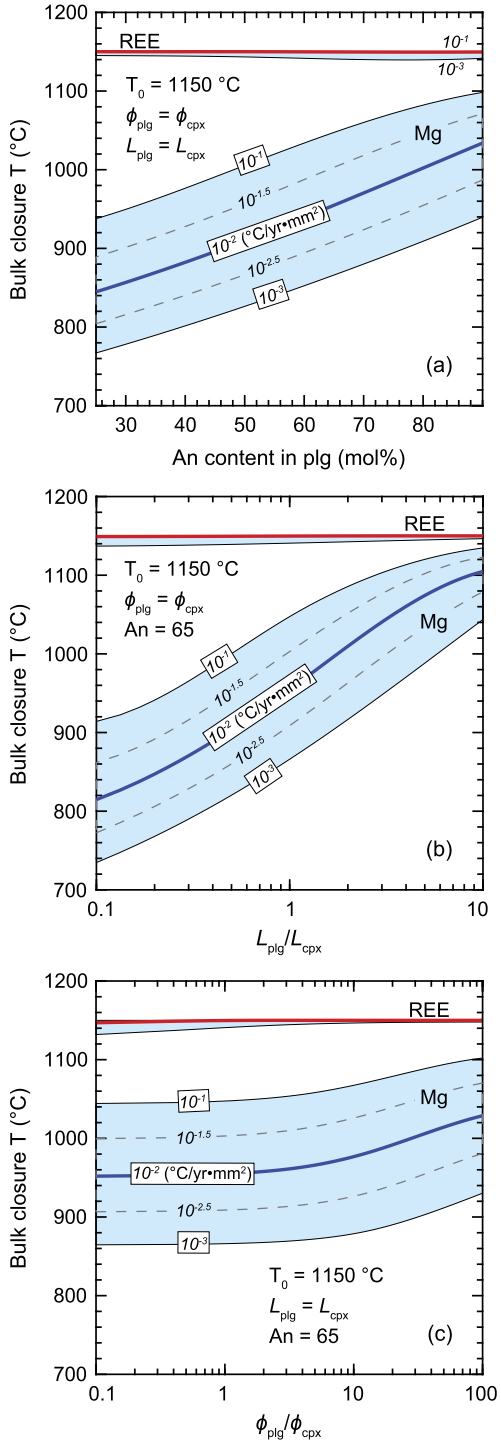

Fig. 4. Plots showing the variations of REE and Mg bulk closure temperatures in plagioclase–clinopyroxene aggregates as a function of anorthite contents in plagioclase (An; (a)), relative grain radii (L_{plg}/L_{cpx}; (b)) and relative mineral modes (ϕ_{plg}/ϕ_{cpx}; (c)). Bulk closure temperatures were calculated using effective cooling rates of 10^{-3}, $10^{-2.5}$, 10^{-2}, $10^{-1.5}$, and 10^{-1} °C/yr·mm^2 (see definition in Appendix A.2) at an initial equilibrium temperature of 1150 °C. Methods of diffusion simulations are outlined in Appendix A, and necessary conditions for different simulations are shown as insets in individual plots.

sion in clinopyroxene for the plagioclase-rich end-member. As Mg diffusion coefficients in clinopyroxene are about one to three orders of magnitude smaller than those in plagioclase (Fig. A.1d), Mg bulk closure temperatures in the plagioclase-rich end-member are significantly greater than those in the clinopyroxene-rich end-member. The closure temperature variations between these two end-members thus show the relative roles of plagioclase and clinopyroxene. Importantly, the dependence of Mg bulk closure temperatures on mineral modals becomes negligible only when $\phi_{plg}/\phi_{cpx} < \sim 2$, indicating the limitation for treating clinopyroxene as an infinite reservoir.

Because of the much faster diffusivities in plagioclase and clinopyroxene, Mg bulk closure temperatures are more responsive than those of REE to changes in cooling rate, composition, mineral mode, and grain radius. Despite the small influences of individual factors, a combination of them may alter REE bulk closure temperatures by >50 °C when the cooling rate is very slow (e.g., <0.001 °C/yr·mm^2). The overall variations of Mg bulk closure temperatures induced by cooling rates, however, are comparable to or even smaller than those due to changes in compositions, mineral modes, or grain sizes. Hence, the knowledge of plagioclase compositions, grain radii, and mineral modes is critical to accurately estimate cooling rates and initial temperatures. The simulation results shown in Fig. 4 can also be used as references for potential errors of bulk closure temperatures as well as cooling rates due to uncertainties in plagioclase compositions, grain radii, and mineral modes.

3. Application to the lower oceanic crust at Hess Deep

The lower oceanic crust at Hess Deep rift valley formed at EPR ~1.3 Myr ago (e.g., Rioux et al., 2012). As a reference section for crust formation at fast-spreading ridges, this cumulate section has been mapped and sampled in several previous studies (e.g., Karson et al., 2002; Lissenberg et al., 2013; Gillis et al., 2014). In particular, the recent study of Lissenberg et al. (2013) reported gabbroic samples with detailed petrographic descriptions, reconstructed stratigraphic depths, and mineral major element compositions. Among those, 15 samples were also analyzed for REE in both plagioclase and clinopyroxene and thus are suitable for applying our new Mg–REE coupled geospeedometer. For accurate determination of cooling rates and initial temperatures, we measured the average grain sizes of plagioclase and clinopyroxene in 46 samples including those with REE data. The average grain sizes of plagioclase were taken as the arithmetic means of average long (length) and short (with) dimensions. Detailed data of the 46 samples are listed in Table S2.

To check the reliability of plagioclase Mg data from Lissenberg et al. (2013), we re-analyzed Mg in plagioclase from 6 representative samples using a wavelength-dispersive detector mounted on a Zeiss Sigma HD field emission gun scanning electron microscope. We used a 20 kV acceleration voltage, high beam current (53 nA), and counting times of 120 s on peak and 60 s off peak. Accuracy and precision was monitored by replicate analysis ($n = 12$) of the Astimex plagioclase standard (Mg = 0.06 wt%), which yielded Mg (wt%) = 0.055 ± 0.004 ($\pm 2\sigma$). The new Mg data for Hess Deep plagioclase correlate very well with the data of Lissenberg et al. (2013) (Fig. S2), indicating that the latter are robust.

3.1. Sample characteristics

The 46 Hess Deep samples cover a reconstructed section of 4.35 km in the lower oceanic crust below the dike-gabbro transition (DGT) and include one tonalite, one diorite, 16 gabbronorites, and 28 (olivine) gabbros with a wide range of mineral modes (ϕ_{plg}/ϕ_{cpx} = 0.9–6.7). The average grain sizes of plagioclase and clinopyroxene are 0.4–4.1 mm and 0.4–5.5 mm, respectively. The compositions of plagioclase and clinopyroxene show complex variations on grain scales, which were attributed to reactive transport of melts through crystal mushes in the lower oceanic crust by Lissenberg et al. (2013) and Lissenberg and MacLeod (2016). To capture the stratigraphic variations of mean mineral compositions,

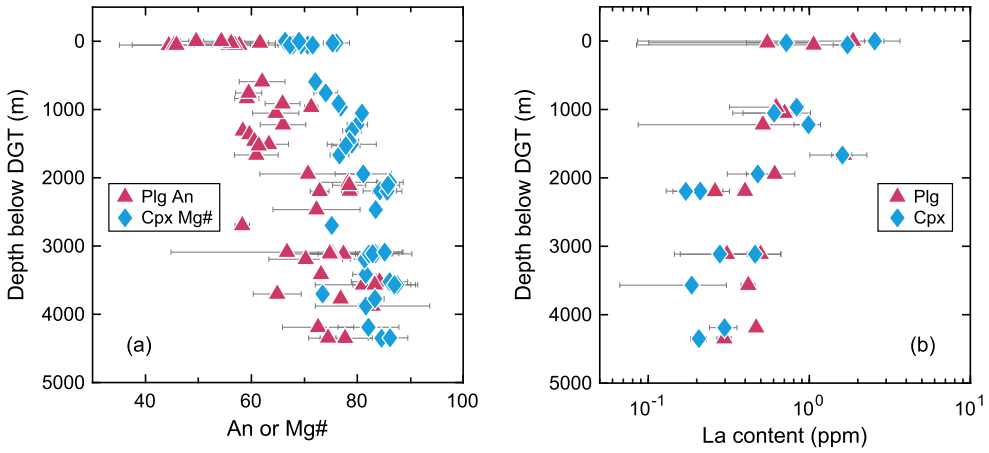

Fig. 5. Stratigraphic variations of averaged major element (a) and REE (b) compositions of plagioclase and clinopyroxene in Hess Deep samples. Depths are the reconstructed stratigraphic positions below the dike-gabbro transition (DGT). Error bars denote the standard errors of the average values, indicating the grain-scale variations of the mineral compositions.

we calculated the average concentrations of major elements and REE in plagioclase and clinopyroxene for individual samples (Table S3). Both rims and cores of mineral grains were taken into account to better represent the average. With decreasing stratigraphic depth (4.35–0 km), anorthite contents in plagioclase decrease from 87.1 to 44.4, the average Mg# in clinopyroxene decrease from 87.5 to 66.4, whereas the average REE concentrations become enriched by about one order of magnitude (e.g., La = 0.17–2.55 ppm in clinopyroxene; La = 0.26–1.87 ppm in plagioclase; Fig. 5). Along the stratigraphy, zigzag patterns appear on the scale of about tens to hundreds of meters.

3.2. Bulk closure temperatures

Applying the Mg- and REE-exchange thermometers to the average mineral compositions, we calculated the bulk closure temperatures of Mg and REE for the Hess Deep samples. Because changing pressure from 0.5 to 2 kbar results in only ~2 °C differences in the calculated temperatures for Mg and REE, an average pressure of 1 kbar was used in all samples. Results of temperature calculations are summarized in Table S2, while the individual calculations of REE bulk closure temperatures are shown in Fig. S3.

The calculated REE closure temperatures for 15 samples with REE data (1040–1283 °C) display a strong positive linear correlation with plagioclase compositions (An = 50–81; red squares in Fig. 6a). The linear relation between REE closure temperatures (T_{REE}) and plagioclase anorthite contents can be simply described through the following expression with a standard error of ±20 °C,

$$T_{REE}\ (^{\circ}C) = 653 + 7.62 \cdot An. \quad (7)$$

Using Eq. (7) we then empirically estimated the analogues of REE closure temperatures for 31 samples without REE data (998 to 1294 °C; An = 45.4–84.2). The calculated Mg closure temperatures (904–1128 °C) for all 46 samples do not show evident correlations with plagioclase anorthite contents (blue circles in Fig. 6a). For the 15 samples with REE data, Mg closure temperatures are 39–320 °C smaller than REE closure temperatures, well below the Dodson limits (Figs. 6b and S3). For 29 samples without REE data, the differences between Mg closure temperatures and the analogues of REE closure temperatures (4–317 °C) are also below the Dodson limits (Figs. 6b and S3). Thus, 44 of the 46 Hess Deep samples are suitable for applying the Mg–REE coupled speedometer.

3.3. Cooling histories

Using the Mg–REE coupled speedometry outlined in Section 2.1, we calculated the initial temperatures and cooling rates for the 44 samples. Errors of the cooling rates were estimated according to the calibration uncertainty (±29 °C) of our Mg-exchange thermometer. Given the small discrepancies (1–16 °C) of Mg bulk closure temperatures derived from the Lissenberg et al. (2013) data and dedicated analyses (Fig. S2 and Table S2), this calibration uncertainty is considered as the maximum errors of Mg bulk closure temperatures. Errors of the initial temperatures are taken from the REE bulk closure temperatures or calculated according to the errors of Mg bulk closure temperatures, among which the larger values were used for individual samples (see reasoning in Fig. S1). The inversion results are listed in Table S2 and are shown as a function of stratigraphic depths in Fig. 6c–d. Inversion calculations are displayed in Fig. S4.

The inverted initial temperatures (998–1353 °C) are slightly greater than the REE closure temperatures and their analogues derived from Eq. (7). The discrepancies for the 15 samples with REE data are less than 14 °C, while those for the 29 samples without REE data appear to be less than 30 °C with one exception (59 °C; JC21-69R-11). The overall smaller differences demonstrate that REE were not subject to extensive diffusive re-distribution in Hess Deep gabbros. Along the stratigraphy, the initial temperatures generally decrease from the bottom up with many small-scale variations. Near the DGT, the initial temperatures cover a broad range (998–1125 °C) within a small depth interval (0–56 m) and are systematically lower than those from below (1096–1353 °C). The highest temperature (1353 ± 60 °C) appears at 3523 m and is 97–133 °C greater than those near the bottom (1220–1256 °C at 4190–4350 m). Interestingly, the temperature variation (1096–1353 °C) at depths of >1900 m is much larger than that from shallower (1097–1156 °C; 593–1666 m).

The inverted cooling rates (0.003–10.2 °C/yr; Fig. 6d) display a ~3.5 orders of magnitude variation across the lower oceanic crust. No evident correlations were found between the cooling rates and plagioclase dimensions (Table S2). Excluding the highest value (10.2 °C/yr) at 2698 m, cooling rates do not show significant differences between samples with or without REE data (0.006–0.80 °C/yr vs. 0.003–2.26 °C/yr). Similar to the initial temperatures, cooling rates near the DGT also show a considerable variation (0.024–2.26 °C/yr) at a narrow depth interval (0–56 m), indicating efficient heat extraction. In addition to the highest value at 2698 m, anomalously rapid cooling rates (0.372–1.13 °C/yr) also appear at 2198–3193 m, suggesting localized high heat extraction

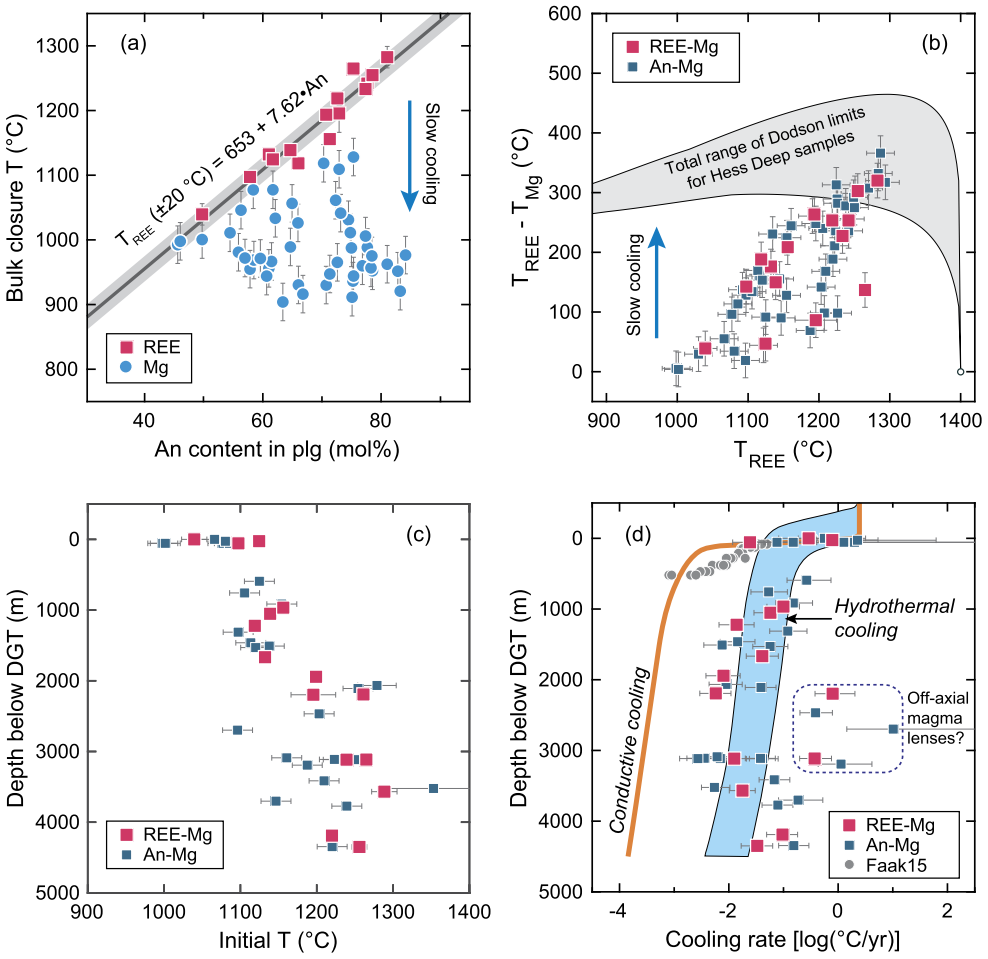

Fig. 6. Plots showing (a) Mg and REE bulk closure temperatures of Hess Deep samples as a function of plagioclase anorthite contents, (b) the closure temperature differences against REE bulk closure temperatures, and (c)–(d) stratigraphic variations of the inverted initial temperatures and cooling rates. The straight line in (a) denotes the linear regression of REE bulk closure temperatures against plagioclase anorthite contents, and the gray region in (a) indicates the ±20 °C standard error. Arrows in (a) and (b) indicate the direction of decreasing cooling rates for a given initial temperature. The grey region in (b) displays the total range of Dodson limits associated with modal abundances and grain sizes of individual Hess Deep samples at an initial temperature of 1400 °C. The conductive (orange curve) and hydrothermal (light blue region) cooling profiles in (d) are taken from the thermal modeling results of Maclennan et al. (2005). *Faak15* in (d) denotes the cooling rates of Hess Deep samples reported in Faak et al. (2015). (For interpretation of the references to color in this figure legend, the reader is referred to the web version of this article.)

rates in the deep lower oceanic crust. With the increase of stratigraphic depth, cooling rates at 593–2066 m manifest an overall decrease from 0.266 to 0.009 °C/yr, whereas those at 3115–4350 m appear to broadly increase from 0.003 to 0.155 °C/yr. Although the Hess Deep samples used in Faak et al. (2015) essentially have no overlaps with ours at depths below DGT, their Mg-in-plagioclase speedometry results (grey dots in Fig. 6d) appear to be systematically lower than the cooling rates of this study, possibly due to the reasons outlined in Introduction. Interestingly, our cooling rates are generally consistent with the Ca-in-olivine speedometry results for Oman ophiolite samples reported in VanTongeren et al. (2008; hollow triangles in Fig. S5) but are about two to three orders of magnitude greater than those of Coogan et al. (2007; hollow diamonds in Fig. S5).

To examine the discrepancies in cooling histories induced by the choice of Mg-exchange thermometers, we also calculated the initial temperatures and cooling rates for our Hess Deep samples using the thermometer of Faak et al. (2013) together with the silica activity model of Faak et al. (2015). Theoretically, Faak et al.'s silica activity model is only valid for gabbros with coexisting olivine and orthopyroxene, which just cover 5 of our 46 samples. Following the assumption of Faak et al. (2015), we applied Faak et al.'s silica activity model to all our Hess Deep samples regardless of the coexistence of olivine and orthopyroxene. Because extrapolation of Faak et al.'s thermometer from their calibration range (1100–1200 °C) to lower temperatures results in systematic underestimations (cf. inset in Fig. 3b), the new set of Mg bulk closure temperatures (787–1100 °C) are about 29–114 °C lower than those derived from Eq. (6) (Table S2; Fig. S6a) and therefore have larger deviations from the REE bulk closure temperatures (Fig. S6b). Consequently, 13 of the 46 samples are above the Dodson limits and hence cannot be used in our speedometer. For the other 33 samples, the new initial temperatures (998–1366 °C) are about 0–138 °C higher than those calculated using our own Mg-exchange thermometer (Eq. (6)), whereas the new cooling rates (0.0003–0.871 °C/yr) are about 0.3–2.4 orders of magnitude lower (Table S2). Stratigraphic variations of the initial temperatures and cooling rates remain similar patterns between the two sets of results (Fig. 6 vs. Fig. S6c–d).

3.4. Implications for ocean crust formation at fast-spreading ridges

The initial temperatures of our samples define the first stratigraphy of cumulate crystallization temperatures for the fast-spreading lower oceanic crust. The lowest temperature (998 ± 20 °C at the DGT) indicates a highly evolved parental melt in the shallow magma chamber beneath the ridge axis, consistent with the low An and Mg# (cf. Fig. 5a) as well as earlier petro-

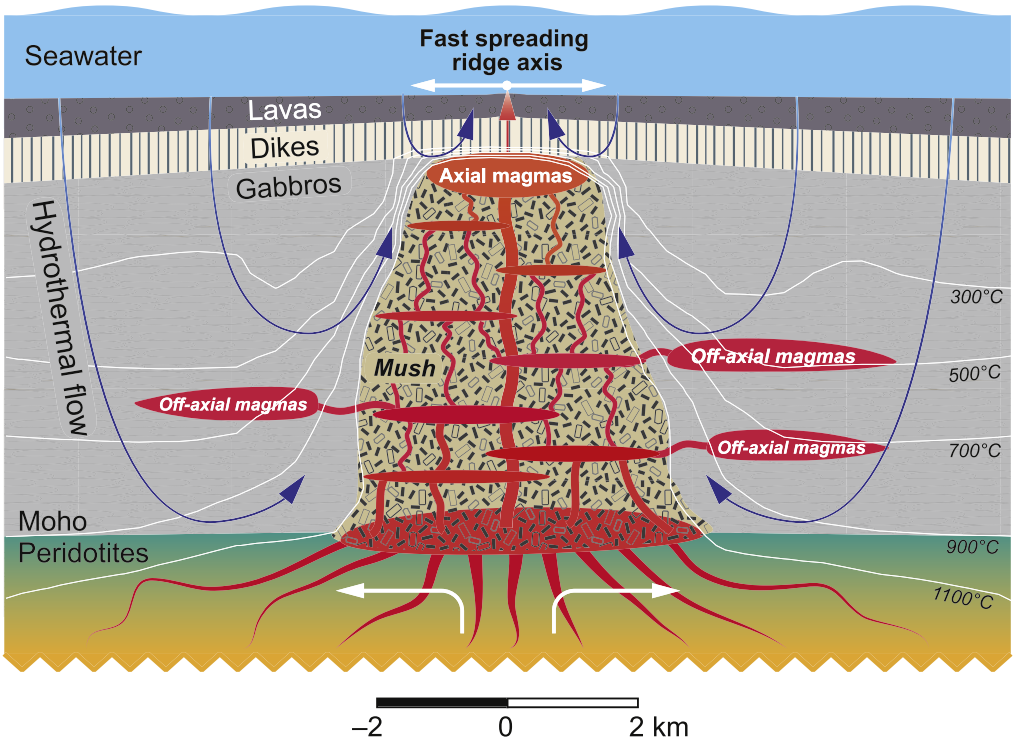

Fig. 7. A schematic illustration of crustal formation beneath fast-spreading mid-ocean ridges. Thin white curves are isotherms from Dunn et al. (2000) showing the thermal structure derived from seismic tomography assuming the effects of anharmonicity and anelasticity. Blue curves with arrows indicate hydrothermal circulations near the ridge axis for efficiently removing heat across the entire crust. Thick white arrows denote the directions of mantle flows and spreading plates. The axial magma chamber is stable during crustal formation, whereas off-axial magma lenses likely solidify on timescales of hundreds to thousands of years except for those with successive melt replenishments. (For interpretation of the references to color in this figure legend, the reader is referred to the web version of this article.)

logical evidence (Natland and Dick, 1996). Given the overall low temperatures at the DGT (998–1125 °C), the magma chamber beneath the ridge axis is likely dominated by continuous replenishment and fractional crystallization of relatively evolved melts from the deeper crust. The highest temperature (1353 ± 60 °C at 3523 m) agrees well with the temperatures of primary MORB basalts (1300–1400 °C; e.g., Lee et al., 2009), indicating the influx of mantle-derived primitive melts in the lower crust. The upward decrease in the initial temperature suggests that the deeper section (>2000 m) confines the temperature of melts delivered shallower. Many small-scale temperature variations in the deeper section may be attributed to vigorous convection of a large, deep-seated cooling magma chamber, which, however, is against the 3-D seismic observations at EPR (e.g., Han et al., 2014). More likely, these small-scale variations indicate accumulation and in situ solidification of replenished melts in small magma bodies (e.g., tens to hundreds of meters) at various depths, as advocated by the multiple-sill model (e.g., Nicolas et al., 1988; Kelemen et al., 1997; Lissenberg et al., 2004; Maclennan et al., 2005; VanTongeren et al., 2008, 2015; Natland and Dick, 2009).

The inverted cooling rates are compatible with the hydrothermal cooling models of Maclennan et al. (2005; Fig. 6d) but about one to two orders of magnitude greater than those derived from the conductive cooling model of Maclennan et al. (2005; Fig. 6d). We note that Maclennan et al.'s hydrothermal models employed adjustable heat extraction rates to match the thermal structures derived from the 2-D seismic tomography in Dunn et al. (2000). Instead, using permeability to explicitly regulate porous hydrothermal flows in the thermal modeling, Cherkaoui et al. (2003) suggested that a permeability of $\sim 4 \times 10^{-14}$ m^2 or greater is required to reproduce the thermal structure of Dunn et al. (2000). Such high permeability could result in cooling rates of ~0.1 °C/yr. Overall, cooling rates derived from both hydrothermal models recover most Hess Deep samples across the lower crust (Fig. 6d). Anomalously rapid cooling rates (0.372–10.2 °C/yr) at 2198–3193 m may be attributed to (1) localized hydrothermal flows induced by faults/shear zones and/or (2) small magma bodies emplaced in the colder off-axial lower crust possibly related to the brittle-ductile transition. Both are equally feasible mechanisms, but recent 3-D seismic observations at EPR (e.g., Han et al., 2014) favor the latter. Although significant uncertainties are likely involved in the thermometer of Faak et al. (2013) at lower temperatures (<1100 °C; see inset in Fig. 3b), cooling rates calculated using Faak et al.'s thermometer remains significantly elevated above the conductive cooling model (cf. Fig. S6d). This indicates that the role of crustal-scale hydrothermal circulations cannot be neglected regardless of the choice of Mg-exchange thermometers.

Together with existing petrological, geochemical and seismic observations, the new speedometry results allow us to delineate a new picture of lower crust formation at fast-spreading mid-ocean ridges (Fig. 7), which involves axial and off-axial magma bodies (e.g., Han et al., 2014) and a crustal-scale mush zone (e.g., Lissenberg et al., 2013; Lissenberg and MacLeod, 2016). As indicated by the stratigraphic variations of cooling histories, the mush zone is supplied by mantle-derived primary melts from the bottom and is efficiently cooled by hydrothermal circulations across the entire lower crust. The replenished melts likely transport reactively through the mush zone, yielding complex zoning in cumulus plagioclase (e.g., Lissenberg et al., 2013). Accumulation and in situ crystallization of replenished melts in small magma bodies at various depths disturb the stratigraphy of cumulus crystallization temperatures. Possibly because of the brittle-ductile transition, the replenished melts may escape from the mush zone to generate off-axial magma lenses. However, high-porosity melt channels also likely appear in the mush zone for delivering relatively primitive melts to the ridge axis (e.g., Natland and Dick, 2009). Assuming a termination temperature of 1000 °C, the mush zone may extend to

~1.5–3.5 km away from the ridge axis according to the thermal structure of Dunn et al. (2000; white curves in Fig. 7).

4. Concluding remarks

Understanding formation of the lower oceanic crust at spreading mid-ocean ridges requires the knowledge of igneous accretion and cooling styles. These two fundamental aspects can be constrained quantitatively using the initial temperatures and cooling rates derived from the newly developed Mg–REE coupled geospeedometry for plagioclase- and clinopyroxene-bearing cumulate rocks. When considered together with geochemical and geophysical observations, results of the Mg–REE speedometry on oceanic cumulates from the lower crust of EPR at Hess Deep reveal that crustal formation at fast-spreading ocean ridges proceeds with hydrothermal circulations across the entire crust, replenishment of mantle-derived melts, and in situ solidification of many small magma bodies at various depths in a crustal-scale mush zone beneath the ridge axis.

Several points, however, are worth of noting for the Mg–REE coupled speedometry. As cooling rates and initial temperatures derived from this speedometer are mean quantities based on bulk (or integrated) diffusion of Mg and REE between coexisting plagioclase and clinopyroxene, average mineral compositions are required for better representing the bulk closure concentrations. The bulk mineral compositions may embrace imprints of melt-rock interaction and/or fractional crystallization to various extents, but the inverted initial temperatures remain meaningful as mean temperatures of latest equilibrium events prior to cooling, considering the very slow diffusion of REE in plagioclase and clinopyroxene (Fig. A.1d). Although Mg and REE diffusivities in plagioclase depend on anorthite contents (Fig. A.1d), it is difficult to quantify the average zoning profiles for bulk diffusion modeling because various plagioclase zonations are often observed in individual gabbros. As different zonations are integrated in the bulk closure concentrations, this bulk-diffusion speedometry practically reduces the overall influence of anorthite zoning from individual plagioclase crystals. In any case, the greatest influence is expected for samples with uniform zoning patterns in all plagioclase crystals. According to the numerical simulations in Sun and Liang (2017), using an averaged composition (An_{68} in their case) for normally zoned plagioclase ($An_{62–77}$) only results in a ~20 °C overestimation in Mg bulk closure temperatures, marking an uncertainty of a factor of two in cooling rates (cf. Fig. 2). Given the 3.5 orders of magnitude variations in cooling rates observed in our samples (Fig. 6d), the effect of anorthite zoning on our speedometry is considered secondary.

Acknowledgements

We thank H. Dick for useful discussions and M. Bickle for editorial advice. Critical comments from K. Faak and an anonymous reviewer helped to improve this manuscript. C. Sun acknowledges support from the Devonshire postdoctoral scholarship at WHOI and NSF grant OCE-1637130. This work was also supported by Natural Environment Research Council (NERC) Grant NE/I001670/1 to J. Lissenberg. R. Dasgupta is greatly appreciated for allowing C. Sun to complete this work at Rice.

Appendix A. Modeling diffusion in plagioclase–clinopyroxene aggregates

A.1. Diffusion model

In a plagioclase–clinopyroxene aggregate, diffusive re-distribution of an element of interest in individual mineral grains can be calculated through the familiar equation,

$$\frac{\partial C_m^j}{\partial t} = \frac{1}{r^{\omega-1}} \frac{\partial}{\partial r}\left(D_m^j \cdot r^{\omega-1} \frac{\partial C_m^j}{\partial r} \right), \tag{A.1}$$

where C is the concentration of an element of interest (j), m denotes plagioclase (plg) or clinopyroxene (cpx), t is time, r is spatial coordinate from the center of the crystal, D is the diffusion coefficient (see Appendix A.4 for the relevant diffusion laws), and ω denotes the geometry (1 for plane sheet, 2 for cylinder, and 3 for sphere). Following the widely used spherical approximation in previous studies (e.g., Eiler et al., 1992; LaTourrette and Wasserburg, 1998; Cherniak, 2003; Van Orman et al., 2014; Watson and Cherniak, 2015), we set $\omega = 3$ in our numerical simulations for the Mg–REE coupled geospeedometer. Assuming fast grain boundary diffusion and mass conservation, the diffusive exchange between the two minerals can be written as

$$\phi_{\mathrm{plg}} \frac{D_{\mathrm{plg}}^j}{L_{\mathrm{plg}}} \frac{\partial C_{\mathrm{plg}}^j}{\partial r}\bigg|_{r=L_{\mathrm{plg}}} = \phi_{\mathrm{cpx}} \frac{D_{\mathrm{cpx}}^j}{L_{\mathrm{cpx}}} \frac{\partial C_{\mathrm{cpx}}^j}{\partial r}\bigg|_{r=L_{\mathrm{cpx}}}, \tag{A.2}$$

where ϕ denotes the mineral modal abundance, and L is the effective grain radius. The mineral modes and grain sizes are assumed to be constant during cooling. For plagioclase (or clinopyroxene) in individual samples, the average grain radius of genetically linked crystals can be taken as the effective grain radius. At the grain boundary between plagioclase and clinopyroxene, the concentrations of the element are determined by its partition coefficient (K),

$$K_{\mathrm{plg/cpx}}^j = \frac{C_{\mathrm{plg}}^j|_{r=L_{\mathrm{plg}}}}{C_{\mathrm{cpx}}^j|_{r=L_{\mathrm{cpx}}}}. \tag{A.3}$$

Eq. (5) was used to describe Mg partition coefficients, while the partitioning model of Sun and Liang (2017) was used to calculate REE partition coefficients. Given the extremely slow diffusion of CaAl–NaSi in plagioclase (Grove et al., 1984) and Al in clinopyroxene (Sautter et al., 1988), the dominant compositional factors (i.e., anorthite in plagioclase and Tschermak components in clinopyroxene) for Mg and REE partitioning can be treated as constants during cooling.

A.2. Cooling path and effective cooling rate

Following Dodson (1973), we described the monotonic cooling profile as a reciprocal function of time in our diffusion simulations,

$$\frac{1}{T} = \frac{1}{T_0} + \eta \cdot t, \tag{A.4}$$

$$\eta = \frac{1}{T_0^2}\frac{dT}{dt}\bigg|_{T_0} = \frac{1}{T_c^2}\frac{dT}{dt}\bigg|_{T_c}, \tag{A.5}$$

where T_0 is the initial temperature of the last equilibrium event; η is a cooling constant determined by the cooling rate (dT/dt) at the initial temperature; and T_c is the bulk closure temperature of the element. Due to the reciprocal relation between temperature and time, cooling rates slightly decrease at lower temperatures and can be adjusted according to equation (A.5).

Since the major interest of diffusion modeling is to extract information of the cooling path, the diffusion equation (Eq. (A.1)) could be rearranged with respective to temperature by applying the chain rule and nondimensionalizing the radial coordinate,

$$\frac{\partial C_m^j}{\partial T} = \left(\frac{1}{L_m^2 dT/dt} \right) \frac{1}{r^2} \frac{\partial}{\partial r}\left(D_m^j \cdot r^2 \frac{\partial C_m^j}{\partial r} \right). \tag{A.6}$$

Note that the product of L^2 and dT/dt can be treated as a single term bearing the meaning of cooling rates for each mineral.

As plagioclase and clinopyroxene often have distinct grain sizes in natural rocks, using the grain radius of clinopyroxene as a reference, we can then define $[L_{cpx}^2 \cdot dT/dt]$ as the *effective cooling rate* (S^*) for the plagioclase–clinopyroxene system. Accordingly, after nondimensionalizing the radial coordinate, diffusion equations for plagioclase and clinopyroxene thus become

$$\frac{\partial C_{plg}^j}{\partial T} = \left(\frac{1}{S^*}\right)\frac{1}{r^2}\frac{\partial}{\partial r}\left(\frac{D_{plg}^j \cdot r^2}{(L_{plg}/L_{cpx})^2}\frac{\partial C_{plg}^j}{\partial r}\right), \tag{A.7a}$$

$$\frac{\partial C_{cpx}^j}{\partial T} = \left(\frac{1}{S^*}\right)\frac{1}{r^2}\frac{\partial}{\partial r}\left(D_{cpx}^j \cdot r^2\frac{\partial C_{cpx}^j}{\partial r}\right). \tag{A.7b}$$

An obvious advantage of this new definition of *effective cooling rate* is that it can simplify the numerical simulations by reducing the three independent factors, dT/dt, L_{cpx}, and L_{plg}, to two variables, S^* and L_{plg}/L_{cpx}.

A.3. Numerical methods

The diffusion equation (Eq. (A.1)) for each crystal in the plagioclase–clinopyroxene aggregate was discretized using a finite difference scheme with both time and space properly centered,

$$\begin{aligned} &-(\varepsilon_{n-1/2}^{i+1})C_{n-1}^{i+1} + (1+\varepsilon_{n-1/2}^{i+1}+\varepsilon_{n+1/2}^{i+1})C_n^{i+1} - (\varepsilon_{n+1/2}^{i+1})C_{n+1}^{i+1} \\ &= (\varepsilon_{n-1/2}^{i})C_{n-1}^{i} + (1-\varepsilon_{n-1/2}^{i}-\varepsilon_{n+1/2}^{i})C_n^{i} + (\varepsilon_{n+1/2}^{i})C_{n+1}^{i}, \end{aligned} \tag{A.8}$$

$$\varepsilon_{n\pm1/2}^{i,cpx} = \frac{\Delta t}{2r_n^2(\Delta r)^2}D_{n\pm1/2}^{i,cpx}r_{n\pm1/2}^2, \tag{A.9}$$

$$\varepsilon_{n\pm1/2}^{i,plg} = \frac{\Delta t}{2r_n^2(\Delta r)^2}\frac{D_{n\pm1/2}^{i,plg}}{(L_{plg}/L_{cpx})^2}r_{n\pm1/2}^2, \tag{A.10}$$

where i and n denote the time and space steps, respectively; Δt is the difference between adjacent time steps; and Δr is the difference between neighboring space steps. Applying this finite-difference scheme with 100 mesh intervals to diffusion in mono-mineral systems, we found that it can reproduce the closure temperatures calculated using the equation of Ganguly and Tirone (1999) to within ±10 °C.

At each time step along the imposed cooling path, we then numerically solved the concentration profiles of both crystals in the plagioclase–clinopyroxene aggregate. The apparent partition coefficient ($\bar{K}$) for element j between the two minerals were then calculated using the following expression,

$$\bar{K}_{plg/cpx}^j = \frac{\frac{1}{L_{plg}^3}\int_0^{L_{plg}} C_{plg}^j dr^3}{\frac{1}{L_{cpx}^3}\int_0^{L_{cpx}} C_{cpx}^j dr^3}, \tag{A.11}$$

where the numerator and denominator indicate the average concentrations of element j in plagioclase and clinopyroxene, respectively. As the rate of diffusive exchange decreases during cooling, the apparent partition coefficient gradually deviates from the equilibrium value and eventually becomes asymptotic, indicating the closure of diffusive exchange. The bulk closure temperature can then be calculated using relevant exchange thermometers and the asymptotic value of apparent partition coefficients. Because heavy- and some middle-REE in plagioclase are often difficult to analyze accurately, the average bulk-closure temperature for light REE is taken as the *measurable* bulk closure temperature of REE.

A.4. Magnesium and REE diffusivities

The diffusive re-distribution of an element (e.g., Mg or REE) in plagioclase or clinopyroxene is a chemical diffusion process driven by the gradient of chemical potential across the crystal. The corresponding diffusion coefficient (i.e., chemical diffusivity; D) is related to the tracer (or self-) diffusion coefficient (D^*) through $D = D^*(1 + \partial \ln\gamma/\partial \ln C)$, where C is the concentration of the element, γ is the activity coefficient, and $(1 + \partial \ln\gamma/\partial \ln C)$ is the thermodynamic factor (e.g., Darken, 1948). Because REE and Mg are trace elements in plagioclase, their thermodynamic factors can be approximately treated as unity, and therefore their tracer (or self-) diffusion coefficients are effectively the chemical diffusion coefficients. This is also the case for REE in clinopyroxene, but does not remain true for Mg in clinopyroxene (e.g., Zhang et al., 2010). Practically, the interdiffusion coefficients of Mg–Fe–Ca in clinopyroxene at the relevant composition are often used as chemical diffusion coefficients for modeling of Mg and Fe diffusion in clinopyroxene (e.g., Müller et al., 2013).

Experimentally measured Mg diffusivities in plagioclase have been reported in three studies (LaTourrette and Wasserburg, 1998; Faak et al., 2013; Van Orman et al., 2014). The diffusion data of LaTourrette and Wasserburg (1998) were collected for a fixed plagioclase composition (An_{95}) at 1200–1400 °C, while those of Faak et al. (2013) were obtained for plagioclase with An_{50-70} at 1100–1200 °C and different silica activities. The Mg diffusion data of Van Orman et al. (2014) cover plagioclase compositions of An_{23-93} and temperatures of 798–1150 °C under silica-saturated conditions and appear to have a strong dependence upon the anorthite content in plagioclase. Using their newly measured diffusion data and those reported in LaTourrette and Wasserburg (1998), Van Orman et al. (2014) developed a generalized Arrhenius equation for Mg diffusion coefficients in plagioclase with An_{23-95} at 798–1400 °C,

$$\ln D_{Mg}^{plg} = -6.06(\pm1.10) - \frac{287(\pm10)\ \text{kJ/mol}}{RT} - 7.96(\pm0.42)X_{An}. \tag{A.12}$$

However, Faak et al. (2013) argued that Mg diffusivities in plagioclase are independent of anorthite contents but are mainly determined by silica activity in addition to temperature. Using their Mg diffusion data for An_{50-70} and 1100–1200 °C and unpublished data from their own group, Faak et al. (2013) calibrated an Arrhenius expression to describe Mg diffusivities in plagioclase as a function of temperature and silica activity,

$$\ln D_{Mg}^{plg} = -9.0 - \frac{321\ \text{kJ/mol}}{RT} - 2.6\ln a_{SiO_2}. \tag{A.13}$$

Note that Eq. (A.13) is the logarithmic form of Eq. (42) of Faak et al. (2013) and that no fitting uncertainties were provided for coefficients in Faak et al.'s original equation.

To further examine the accuracies of these two models (Eqs. (A.12)–(A.13)), we applied both to existing Mg diffusivities from the aforementioned experimental studies (Fig. A.1a–b). The model of Faak et al. (2013; Eq. (A.13)) generally reproduces the Mg diffusivities from their own experiments (An = 50–70) as well as those from Van Orman et al. (2014) for An_{43} and An_{67} (Fig. A.1b); however, significant discrepancies appear in the diffusion data for An_{23} and An_{93}. The model of Van Orman et al. (2014; Eq. (A.12)) well reproduces the Mg diffusivities used for their model calibration (LaTourrette and Wasserburg, 1998; Van Orman et al., 2014) as well as those from diffusion experiments of Faak et al. (2013) with excess silica (Fig. A.1a); however, systematic overestimations

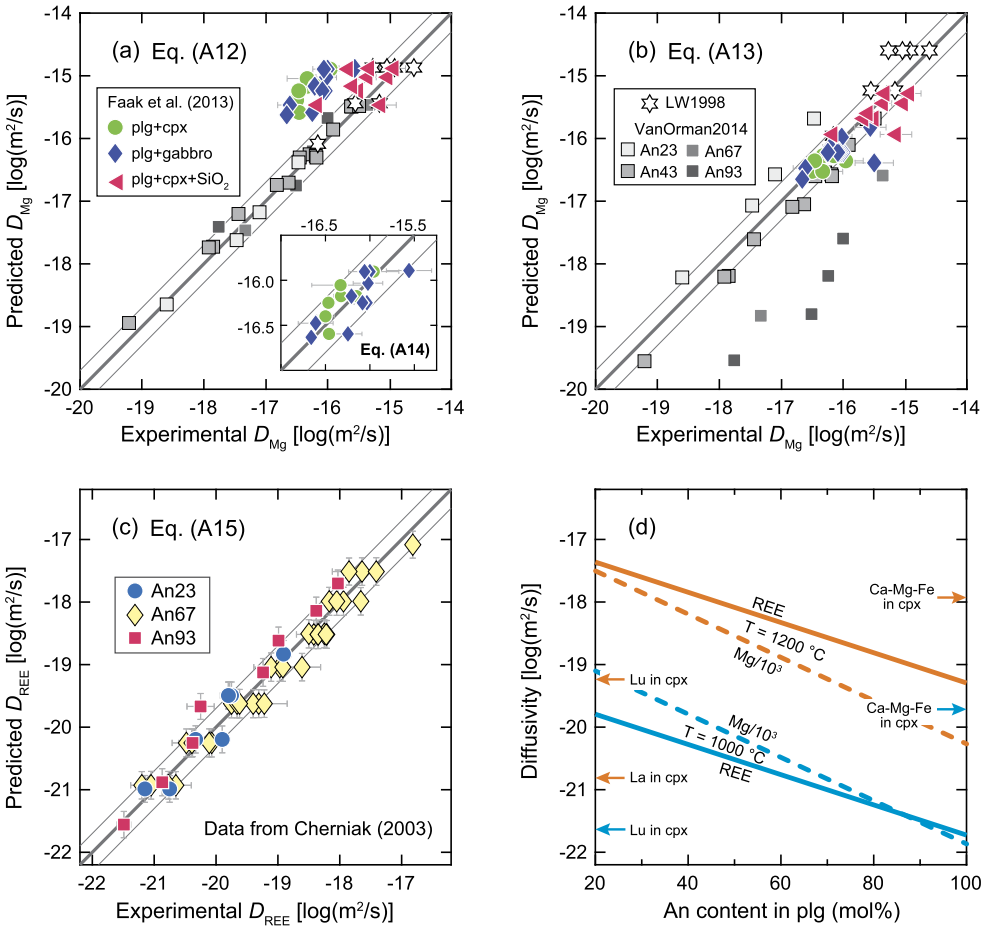

Fig. A.1. Comparisons between model-predicted diffusion coefficients of Mg (a–b) and REE (c) in plagioclase and experimentally determined values from diffusion experiments in the literature, and Arrhenius plot (d) showing Mg (dashed lines; Eq. (A.14)) and REE diffusion coefficients in plagioclase (solid lines; Eq. (A.12)) as a function of anorthite content in plagioclase at 1200 °C (orange) and 1000 °C (blue). Dark grey lines in (a–c) indicate the 1:1 correlation lines, while thin grey lines outline a factor of two variations. Error bars show the uncertainties reported in the literature (a–c) as well as the standard errors derived from the regression analyses (c). LW1998 denotes the data from LaTourrette and Wasserburg (1998). For comparison, Mg diffusion coefficients in plagioclase are reduced by three orders of magnitude in (d). Arrows in (d) denote Mg (Müller et al., 2013) and REE diffusion coefficients (Van Orman et al., 2001) in clinopyroxene at 1200 °C (orange) and 1000 °C (blue). (For interpretation of the references to color in this figure legend, the reader is referred to the web version of this article.)

are manifested by the silica-free experiments of Faak et al. (2013). We note that the overestimations of the silica-free diffusion data by Van Orman et al.'s model are 1.01 ± 0.18 orders of magnitude, independent of the coexisting matrixes (clinopyroxene or gabbro) of plagioclase. Therefore, we can describe all existing Mg diffusion data for plagioclase through a modified expression of Van Orman et al. (2014),

$$\ln D_{\mathrm{Mg}}^{\mathrm{plg}} = -6.06(\pm 1.10) - \frac{287(\pm 10)\ \mathrm{kJ/mol}}{RT} - 7.96(\pm 0.42)X_{\mathrm{An}} - 2.33(\pm 0.41)(1-\delta), \tag{A.14}$$

where δ is a step function indicating the absence ($\delta = 0$) or presence ($\delta = 1$) of silica in the petrological system. As silica is not a typical mineral in oceanic gabbros, δ in Eq. (A.14) is set as zero for our diffusion modeling.

The only existing REE diffusion data for plagioclase were experimentally measured in Cherniak (2003) for three different plagioclase crystals (An_{23}, An_{66}, and An_{93}) at 925–1350 °C. A striking feature of the REE diffusion data is their strong negative correlation with the anorthite content in plagioclase. Through multiple linear regression analysis, we found that all REE diffusion data from Cherniak (2003) can be described by the following Arrhenius equation,

$$\ln D_{\mathrm{REE}}^{\mathrm{plg}} = -3.21(\pm 2.55) - \frac{437(\pm 26)\ \mathrm{kJ/mol}}{RT} - 5.56(\pm 0.84)X_{\mathrm{An}}. \tag{A.15}$$

REE diffusion coefficients predicted by Eq. (A.15) differ from the experimentally determined values generally by within a factor of two (Fig. A.1c). The differences are comparable to the reported uncertainties in Cherniak (2003). Eq. (A.15) is then used in our diffusion model (Eq. (A.1)) to simulate REE diffusion in plagioclase. Interestingly, Mg and REE diffusion coefficients in plagioclase show similar dependence on plagioclase anorthite contents, but the absolute values of the former are greater than those of the latter by ~2–4 orders of magnitude (Fig. A.1d).

Interdiffusion coefficients of Ca–Mg–Fe in clinopyroxene were measured in three experimental studies (Brady and McCallister, 1983; Dimanov and Wiedenbeck, 2006; Müller et al., 2013). The recent measurements of Müller et al. (2013) for diopside (X_{Ca} = 1.0 per six-oxygen) at 1 atm are similar to those of Dimanov and Wiedenbeck (2006); however, both are about one order of magnitude greater than Brady and McCallister's measurements. The differences may be attributed to the low-Ca clinopyroxene used in Brady and McCallister (1983) ($X_{\mathrm{Ca}} = 0.5$ per six-oxygen) or perhaps to the higher pressure (2.5 GPa) of Brady and McCallister's experiments. Nevertheless, Müller et al.'s diffusion data cover a broader range of temperatures and are more relevant to oceanic gabbros regarding the clinopyroxene composition and pressure.

Thus, the Arrhenius expression of Müller et al. (2013) is used in our diffusion model to simulate Mg diffusion in clinopyroxene. With the increase of anorthite content in plagioclase (e.g., An = 20–100), the relative differences in Mg diffusivities between clinopyroxene and plagioclase are reduced from about three orders of magnitude to less than a factor of two (Fig. A.1d).

Tracer diffusion coefficients of REE in clinopyroxene have been reported in two experimental studies (Sneeringer et al., 1984; Van Orman et al., 2001). With a more complete list of REE in a natural clinopyroxene crystal, Van Orman and coworkers showed that REE diffusion coefficients in clinopyroxene decrease systematically with the increase of REE ionic radii (Fig. A.1d). The compositional effect, if any, on REE diffusivities in clinopyroxene is unknown due to the lack of diffusion data for variable clinopyroxene compositions. Thus, the Arrhenius equations of Van Orman et al. (2001) for individual REE are then implemented in our diffusion model to describe REE diffusivities in clinopyroxene, which are generally greater than those in plagioclase by up to three orders of magnitude (Fig. A.1d). Compared with the interdiffusion coefficients of Ca–Mg–Fe from Müller et al. (2013), REE diffusivities in clinopyroxene are ~1–3 orders of magnitude smaller (Fig. A.1d).

Appendix B. Supplementary material

Supplementary material related to this article can be found online at https://doi.org/10.1016/j.epsl.2018.01.032.

References

Brady, J.B., McCallister, R.H., 1983. Diffusion data for clinopyroxenes from homogenization and self-diffusion experiments. Am. Mineral. 68, 95–105.

Carmichael, I.S.E., 2004. The activity of silica, water, and the equilibration of intermediate and silicic magmas. Am. Mineral. 89, 1438–1446.

Cherkaoui, A.S., Wilcock, W.S., Dunn, R.A., Toomey, D.R., 2003. A numerical model of hydrothermal cooling and crustal accretion at a fast spreading mid-ocean ridge. Geochem. Geophys. Geosyst. 4 (9). https://doi.org/10.1029/2001GC000215.

Cherniak, D.J., 2003. REE diffusion in feldspar. Chem. Geol. 193, 25–41.

Coogan, L.A., Jenkin, G.R.T., Wilson, R.N., 2007. Contrasting cooling rates in the lower oceanic crust at fast- and slow-spreading ridges revealed by geospeedometry. J. Petrol. 48, 2211–2231.

Costa, F., Chakraborty, S., Dohmen, R., 2003. Diffusion coupling between trace and major elements and a model for calculation of magma residence times using plagioclase. Geochim. Cosmochim. Acta 67, 2189–2200.

Darken, L.S., 1948. Diffusion, mobility and their interrelation through free energy in binary metallic systems. Trans. AIME 175, 184–194.

Dick, H.J.B., Tivey, M.A., Tucholke, B.E., 2008. Plutonic foundation of a slow-spreading ridge segment: oceanic core complex at Kane Megamullion, 23°30′N, 45°20′W. Geochem. Geophys. Geosyst. 9 (5). https://doi.org/10.1029/2007GC001645.

Dimanov, A., Wiedenbeck, M., 2006. (Fe, Mn)–Mg interdiffusion in natural diopside: effect of pO_2. Eur. J. Mineral. 18, 705–718.

Dodson, M.H., 1973. Closure temperature in cooling geochronological and petrological systems. Contrib. Mineral. Petrol. 40, 259–274.

Dunn, R.A., Toomey, D.R., Solomon, S.C., 2000. Three-dimensional seismic structure and physical properties of the crust and shallow mantle beneath the East Pacific Rise at 9°30′N. J. Geophys. Res., Solid Earth 105, 23537–23555.

Ehlers, K., Powell, R., 1994. An empirical modification of Dodson's equation for closure temperature in binary systems. Geochim. Cosmochim. Acta 58, 241–248.

Eiler, J.M., Baumgartner, L.P., Valley, J.W., 1992. Intercrystalline stable isotope diffusion: a fast grain boundary model. Contrib. Mineral. Petrol. 112, 543–557.

Faak, K., Chakraborty, S., Coogan, L.A., 2013. Mg in plagioclase: experimental calibration of a new geothermometer and diffusion coefficients. Geochim. Cosmochim. Acta 123, 195–217.

Faak, K., Coogan, L.A., Chakraborty, S., 2015. Near conductive cooling rates in the upper-plutonic section of crust formed at the East Pacific Rise. Earth Planet. Sci. Lett. 423, 36–47.

Ganguly, J., Tirone, M., 1999. Diffusion closure temperature and age of a mineral with arbitrary extent of diffusion: theoretical formulation and applications. Earth Planet. Sci. Lett. 170, 131–140.

Gillis, K.M., Snow, J.E., Klaus, A., et al., 2014. Primitive layered gabbros from fast-spreading lower oceanic crust. Nature 505, 204–207.

Grove, T.L., Baker, M.B., Kinzler, R.J., 1984. Coupled CaAl–NaSi diffusion in plagioclase feldspar: experiments and applications to cooling rate speedometry. Geochim. Cosmochim. Acta 48, 2113–2121.

Grove, T.L., Kinzler, R.J., Bryan, W.B., 1992. Fractionation of mid-ocean ridge basalt (MORB). In: Phipps Morgan, J., Blackman, D.K., Sinton, J.M. (Eds.), Mantle Flow and Melt Generation at Mid-Ocean Ridges. American Geophysical Union, Washington, D.C., pp. 281–310.

Han, S., Carbotte, S.M., Carton, H., Mutter, J.C., Aghaei, O., Nedimović, M.R., Canales, J.P., 2014. Architecture of on- and off-axis magma bodies at EPR 9°37–40′N and implications for oceanic crustal accretion. Earth Planet. Sci. Lett. 390, 31–44.

Holland, T., Powell, R., 1992. Plagioclase feldspars: activity-composition relations based upon Darken's quadratic formalism and Landau theory. Am. Mineral. 77, 53–61.

Karson, J.A., Klein, E.M., Hurst, S.D., Lee, C., Rivizzigno, P., Curewitz, D., Morris, A.R., Hess Deep Science Party, 2002. Structure of uppermost fast-spread oceanic crust exposed at the Hess Deep Rift: implications for subaxial processes at the East Pacific Rise. Geochem. Geophys. Geosyst. 2002 (3). https://doi.org/10.1029/2001GC000155.

Kelemen, P.B., Koga, K., Shimizu, N., 1997. Geochemistry of gabbro sills in the crust-mantle transition zone of the Oman ophiolite: implications for the origin of the oceanic lower crust. Earth Planet. Sci. Lett. 146, 475–488.

LaTourrette, T., Wasserburg, G.J., 1998. Mg diffusion in anorthite: implications for the formation of early solar system planetesimals. Earth Planet. Sci. Lett. 158, 91–108.

Lee, C.T.A., Luffi, P., Plank, T., Dalton, H., Leeman, W.P., 2009. Constraints on the depths and temperatures of basaltic magma generation on Earth and other terrestrial planets using new thermobarometers for mafic magmas. Earth Planet. Sci. Lett. 279, 20–33.

Liang, Y., 2014. Time scales of diffusive re-equilibration in bi-mineralic systems with and without a fluid or melt phase. Geochim. Cosmochim. Acta 132, 274–287.

Liang, Y., 2017. Effect of pressure on closure temperature of a trace element in cooling petrological systems. Contrib. Mineral. Petrol. 172, 8. https://doi.org/10.1007/s00410-016-1327-8.

Lissenberg, C.J., Bedard, J.H., van Staal, C.R., 2004. The structure and geochemistry of the gabbro zone of the Annieopsquotch ophiolite, Newfoundland: implications for lower crustal accretion at spreading ridges. Earth Planet. Sci. Lett. 229, 105–123.

Lissenberg, C.J., MacLeod, C.J., 2016. A reactive porous flow control on mid-ocean ridge magmatic evolution. J. Petrol. 57, 2195–2220.

Lissenberg, C.J., MacLeod, C.J., Howard, K.A., Godard, M., 2013. Pervasive reactive melt migration through fast-spreading lower oceanic crust (Hess Deep, equatorial Pacific Ocean). Earth Planet. Sci. Lett. 361, 436–447.

Maclennan, J., Hulme, T., Singh, S.C., 2005. Cooling of the lower oceanic crust. Geology 33, 357–366.

Müller, T., Dohmen, R., Becker, H.W., Ter Heege, J.H., Chakraborty, S., 2013. Fe–Mg interdiffusion rates in clinopyroxene: experimental data and implications for Fe–Mg exchange geothermometers. Contrib. Mineral. Petrol. 166, 1563–1576.

Natland, J.H., Dick, H.J.B., 1996. Melt migration through high-level gabbroic cumulates of the East Pacific Rise at Hess Deep: the origin of magma lenses and the deep crustal structure of fast-spreading ridges. In: Mével, C., Gillis, K., Allan, J.F., Meyer, P.S. (Eds.), Proceedings of the Ocean Drilling Program, Scientific Results, vol. 147. Ocean Drilling Program, College Station, TX, pp. 21–58.

Natland, J.H., Dick, H.J., 2009. Paired melt lenses at the East Pacific Rise and the pattern of melt flow through the gabbroic layer at a fast-spreading ridge. Lithos 112, 73–86.

Nicolas, A., Reuber, I., Benn, K., 1988. A new magma chamber model based on structural studies in the Oman ophiolite. Tectonophysics 151, 87–105.

Phipps Morgan, J., Chen, Y.J., 1993. The genesis of oceanic crust: magma injection, hydrothermal circulation, and crustal flow. J. Geophys. Res., Solid Earth 98, 6283–6297.

Quick, J.E., Denlinger, R.P., 1993. Ductile deformation and the origin of layered gabbro in ophiolites. J. Geophys. Res., Solid Earth 98, 14015–14027.

Rioux, M., Lissenberg, C.J., McLean, N.M., Bowring, S.A., MacLeod, C.J., Hellebrand, E., Shimizu, N., 2012. Protracted timescales of lower crustal growth at the fast-spreading East Pacific Rise. Nat. Geosci. 5, 275–278.

Sautter, V., Jaoul, O., Abel, F., 1988. Aluminum diffusion in diopside using the $^{27}Al(p,\gamma)^{28}Si$ nuclear reaction: preliminary results. Earth Planet. Sci. Lett. 89, 109–114.

Sneeringer, M., Hart, S.R., Shimizu, N., 1984. Strontium and samarium diffusion in diopside. Geochim. Cosmochim. Acta 48, 1589–1608.

Sun, C., Graff, M., Liang, Y., 2017. Trace element partitioning between plagioclase and silicate melt: the importance of temperature and plagioclase composition, with implications for terrestrial and lunar magmatism. Geochim. Cosmochim. Acta 206, 273–295.

Sun, C., Liang, Y., 2012. Distribution of REE between clinopyroxene and basaltic melt along a mantle adiabat: effects of major element composition, water, and temperature. Contrib. Mineral. Petrol. 163, 807–823.

Sun, C., Liang, Y., 2017. A REE-in-plagioclase–clinopyroxene thermometer for crustal rocks. Contrib. Mineral. Petrol. 172, 24. https://doi.org/10.1007/s00410-016-1326-9.

Van Orman, J.A., Cherniak, D.J., Kita, N.T., 2014. Magnesium diffusion in plagioclase: dependence on composition, and implications for thermal resetting of the ^{26}Al–^{26}Mg early solar system chronometer. Earth Planet. Sci. Lett. 385, 79–88.

Van Orman, J.A., Grove, T.L., Shimizu, N., 2001. Rare earth element diffusion in diopside: influence of temperature, pressure, and ionic radius, and an elastic model for diffusion in silicates. Contrib. Mineral. Petrol. 141, 687–703.

VanTongeren, J.A., Hirth, G.R.E.G., Kelemen, P.B., 2015. Constraints on the accretion of the gabbroic lower oceanic crust from plagioclase lattice preferred orientation in the Samail ophiolite. Earth Planet. Sci. Lett. 427, 249–261.

VanTongeren, J.A., Kelemen, P.B., Hanghøj, K., 2008. Cooling rates in the lower crust of the Oman ophiolite: Ca in olivine, revisited. Earth Planet. Sci. Lett. 267, 69–82.

Watson, E.B., Cherniak, D.J., 2015. Quantitative cooling histories from stranded diffusion profiles. Contrib. Mineral. Petrol. 169, 57. https://doi.org/10.1007/s00410-015-1153-4.

Yao, L., Liang, Y., 2015. Closure temperature in cooling bi-mineralic systems: I. Definition and with application to REE-in-two-pyroxene thermometer. Geochim. Cosmochim. Acta 162, 137–150.

Zhang, X., Ganguly, J., Ito, M., 2010. Ca–Mg diffusion in diopside: tracer and chemical inter-diffusion coefficients. Contrib. Mineral. Petrol. 159, 175–186.